SANDIA REPORT

SAND2016-10703
Unlimited Release
Printed September 2016

Measurement of Laser Weld Temperatures for 3D Model Input

Daryl J. Dagel, Grant D. Grossetete, Danny O. Maccallum

Prepared by
Sandia National Laboratories
Albuquerque, New Mexico 87185 and Livermore, California 94550

Sandia National Laboratories is a multi-mission laboratory managed and operated by Sandia Corporation, a wholly owned subsidiary of Lockheed Martin Corporation, for the U.S. Department of Energy's National Nuclear Security Administration under contract DE-AC04-94AL85000.

Issued by Sandia National Laboratories, operated for the United States Department of Energy by Sandia Corporation.

Available to DOE and DOE contractors from
U.S. Department of Energy
Office of Scientific and Technical Information
P.O. Box 62
Oak Ridge, TN 37831

Telephone: (865) 576-8401
Facsimile: (865) 576-5728
E-Mail: reports@osti.gov
Online ordering: http://www.osti.gov/scitech

Available to the public from
U.S. Department of Commerce
National Technical Information Service
5301 Shawnee Rd
Alexandria, VA 22312

Telephone: (800) 553-6847
Facsimile: (703) 605-6900
E-Mail: orders@ntis.gov
Online order: http://www.ntis.gov/search

SAND2016-10703
Unlimited Release
Printed September 2016

Measurement of Laser Weld Temperatures for 3D Model Input

Daryl J. Dagel, Grant D. Grossetete, Danny O. Maccallum
Sandia National Laboratories
P.O. Box 5800
Albuquerque, New Mexico 87185-MS1080

Abstract

Laser welding is a key joining process used extensively in the manufacture and assembly of critical components for several weapons systems. Sandia National Laboratories advances the understanding of the laser welding process through coupled experimentation and modeling. This report summarizes the experimental portion of the research program, which focused on measuring temperatures and thermal history of laser welds on steel plates. To increase confidence in measurement accuracy, researchers utilized multiple complementary techniques to acquire temperatures during laser welding. This data serves as input to and validation of 3D laser welding models aimed at predicting microstructure and the formation of defects and their impact on weld-joint reliability, a crucial step in rapid prototyping of weapons components.

ACKNOWLEDGMENTS

The authors wish to thank Peter Duran, Pierrette Gorman, Mike Maguire, Mark Reece, Jeff Rodelas, and Shelley Williams, for their help, guidance, and services during the execution of this project.

The authors also wish to thank Mario Martinez, whose feedback and expertise on the 3D modeling research at SNL helped guide the thermal diagnostic experiments.

In addition, the authors acknowledge David Surmick and Xianglei Mao for their help and expertise in understanding plasma spectroscopy.

Finally, the authors gratefully acknowledge the mentorship and management of the project by Olga Spahn and Diane Peebles.

CONTENTS

FIGURES

1. INTRODUCTION

Laser welding of metals is a fusion welding technique that is achieved by focusing a high power laser beam (100s W to kWs) to a small spot (100s μm). At low power, the absorbed laser energy conducts through a shallow region and creates a melt pool. At higher power, however, the laser energy produces an ionized metal vapor (plasma), which rapidly accelerates the absorption of energy through the development of a so-called keyhole, a deep and narrow cavity drilled by the laser (see Fig. 1). Whereas in conduction only welding where the absorption is <50%, the keyhole effect increases the absorption to as much as ~80% [1].

Major challenges in laser welds for weapons manufacturing include porosity formation and weld morphology [2]. Modeling in combination with experiment provides an effective means to understand and control laser welding to meet design specifications. Successful completion of these experiments and models will ultimately lead to joint qualification and verification before and during manufacture.

The goal of this project was to provide experimental data needed for validation, boundary condition determination and sub-model tuning (e.g. laser-metal-surface interactions) of a generalized 3D laser-weld modeling capability. Together with on-line metrology, these weld process models form the basis of a rapid prototyping capability.

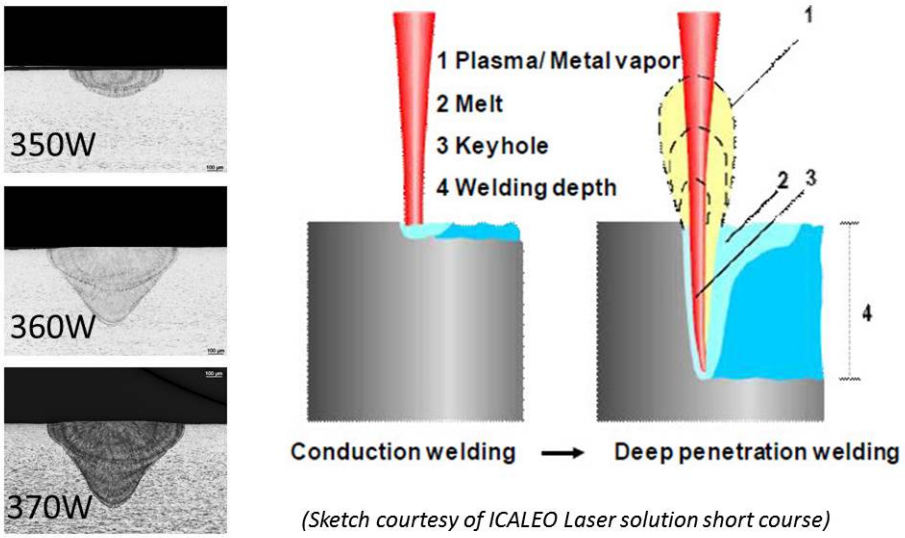

Figure 1. Schematic of bead-on-plate, traveling laser weld. A moving plate underneath the focused high-power laser beam absorbs a fraction of the incident power, which melts a region around the laser focus. A comet-like tail develops on the trailing side of the weld due to the motion. At a characteristic power, the laser vaporizes (and ionizes) the plate material generating a plasma and cavity (keyhole) as a result of the vapor pressure pushing the molten material away from the focus. The weld penetration increases dramatically after this nonlinear transition, as shown in the cross-sections for 80 ipm stage speed.

2. THERMAL DIAGNOSTICS

2.1. Overview

Temperature measurements of laser-metal processing are routinely accomplished with thermocouples, infrared cameras, and pyrometers [3]. However, the demand for accurate, high spatial and temporal resolution temperature data presents significant challenges for experimentalists, where the temperatures, gradients and heating/cooling rates are extreme [4]. For example, in laser welding of metals, the small size and high speed of the melt pool make thermocouples only sufficient for measuring temperatures along boundaries. Infrared cameras also have limitations in this environment because of the low and changing emissivity of the hot metal, where the deduced temperatures are apparent (or relative) temperatures and not true (or absolute) temperatures. Schemes that alter the emissivity to a known value (e.g. coating the surface with high emissivity paint) prove useful in this context.

2.2. Techniques

2.2.1. Infrared (IR) Imaging

Infrared (IR) thermal imaging (or thermography) is the use of an IR camera to measure the apparent temperature of an object derived from its radiance and emissivity [5]. A common wavelength band for IR cameras to operate is the 3-5 μm mid-wave IR band (MWIR), owing to the good atmospheric transparency in that window. For an unknown object, the IR camera integrates the response across this band and, comparing it to a calibration standard (blackbody), provides radiance. This can be converted to surface temperature if the emissivity of the object is known.

The spectral radiance of a blackbody (emissivity ε=1) is given by Planck's law:

$$E_\lambda(T) = \frac{C_1}{\lambda^5}\frac{1}{e^{C_2/\lambda T}-1}, \tag{1}$$

where $C_1 = 3.742\times10^8$ W-μm^4/m^2 and $C_2 = 14388$ μm-K. In Fig. 2, this radiance is plotted from 400-3000 nm from 500 °C to 3500 °C. As shown, the radiance differs by several orders of magnitude, which highlights the need for high dynamic range diagnostic instruments, especially in the visible spectrum. For wavelengths and temperatures on the blue (shorter wavelength) side of the peak, Wien's approximation can be used to eliminate the factor of 1 in Eq. (1). This approximation has an error less than 1% for $\lambda T < 3130$ μm-K [6]. Thus, minimal error in temperature is introduced for temperatures as high as 3130 K at 1000 nm and 7825 K at 400 nm.

Of course, real objects radiate less than a blackbody, and their emissivity varies according to several inter-related properties, including wavelength, temperature, degree of oxidation, surface roughness, material state (e.g. solid, liquid, powder), and angle of incidence [5]. Making use of Wien's approximation, an equation for the measured signal $I_\lambda(T)$ of an object at wavelength λ can be written:

$$I_\lambda(T) = \sigma_\lambda \frac{C_1}{\lambda^5} \frac{\varepsilon_\lambda(T)}{e^{C_2/\lambda T}}, \tag{2}$$

where σ_λ is an instrument dependent factor that includes optical transmission losses and detector sensitivity. If reflected background radiance and atmospheric transmission losses are neglected, Eq. (2) represents the total radiation emitted by the object actually detected by the instrument and through appropriate calibrations can be used to find absolute temperatures.

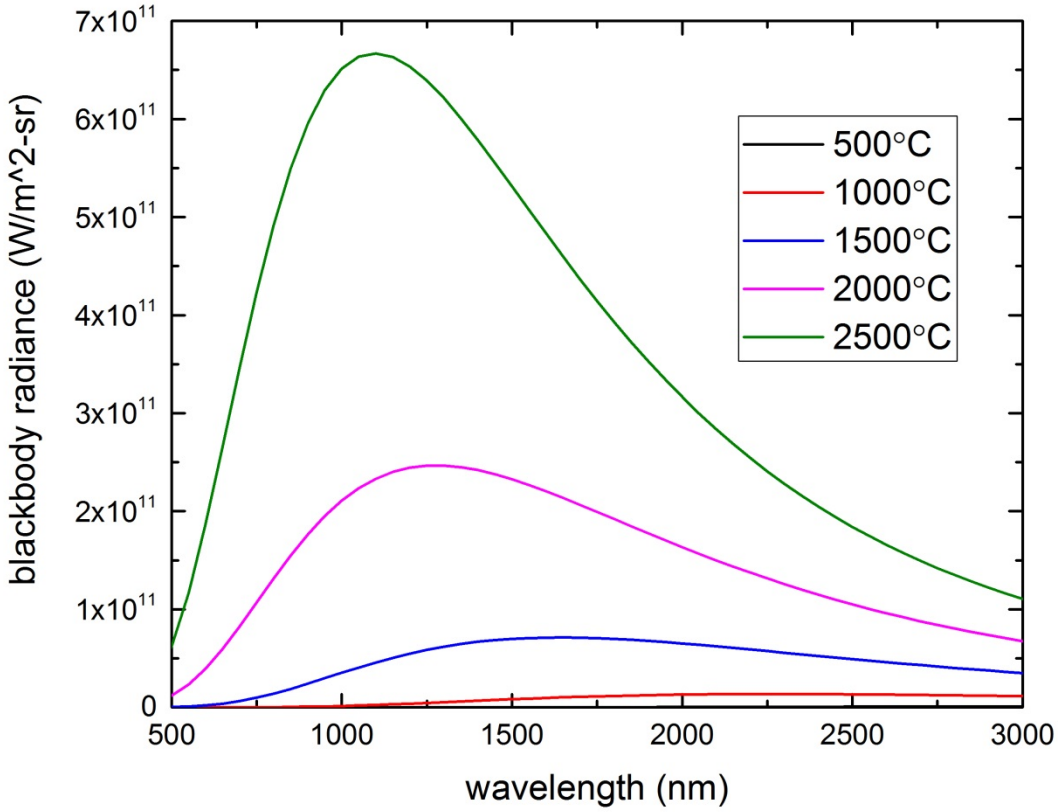

Figure 2. Calculated spectral radiance of a blackbody source at five different temperatures spanning the visible and near IR spectrum. MWIR cameras work between 3-5 μm, where the demand for high dynamic range instruments is not as great.

2.2.2. 2-Color and 4-Color Pyrometry

Equation 2 is useful only when the emissivity is well characterized, which is rare for metals undergoing laser processing. The advantage of 2-color thermography is that measurements of absolute temperature are possible without knowledge of the emissivity. Errors arise only when the gray body assumption does not hold (i.e. when the emissivities differ at the two operating wavelengths of the pyrometer). Taking the ratio of the measured signal at λ_1 and λ_2 gives

$$R_{12} = \sigma_{12} \frac{\varepsilon_1(T)}{\varepsilon_2(T)} \left(\frac{\lambda_2}{\lambda_1} \right)^5 e^{\frac{C_2}{T}\left(\frac{1}{\lambda_2} - \frac{1}{\lambda_1}\right)}, \tag{3}$$

where σ_{12} represents the combined throughput response deduced from a blackbody calibration. Inverting Eq. (3) with $\varepsilon_1=\varepsilon_2$ results in an expression for the ratio temperature:

$$T_R = \left(\frac{\ln R_{12} - \ln\left[\sigma_{12}(\lambda_2/\lambda_1)^5\right]}{C_2\left(\lambda_2^{-1} - \lambda_1^{-1}\right)} \right)^{-1}. \tag{4}$$

This differs from the true temperature T by

$$T = \left(\frac{1}{T_R} - \frac{\ln(\varepsilon_1/\varepsilon_2)}{C_2\left(\lambda_2^{-1} - \lambda_1^{-1}\right)} \right)^{-1}. \tag{5}$$

Thus, the error for the 2-color approach depends on the emissivity ratio and on the selected wavelengths, with the two terms working contrary to each other.

For economic reasons, commercial pyrometers operate with silicon, CMOS detectors (400-900 μm). But a pyrometer designed for laser welding would ideally measure temperatures between room temperature and ~3000 °C (the peak temperature at the center of a superheated weld pool [7]). Unfortunately, this is not practical given the $>10^{20}$ difference in radiance between those temperatures in the visible spectrum (see Fig. 2). Extending the dynamic range of a visible pyrometer motivated the development of a 4-color pyrometer.

This new instrument (Fig. 3) consists of four, high-sensitivity silicon CMOS cameras configured as two independent 2-color pyrometers combined in a common hardware assembly [8]. This coupling of pyrometers permits low and high temperature regions to be targeted within the silicon response curve, thereby broadening the dynamic range of the instrument. Also, by utilizing the high dynamic range features of the CMOS cameras, the response gap between the two wavelength bands can be bridged. Together these hardware and software enhancements are predicted to expand the real-time temperature response of the 4-color pyrometer from 600 °C to 3000 °C.

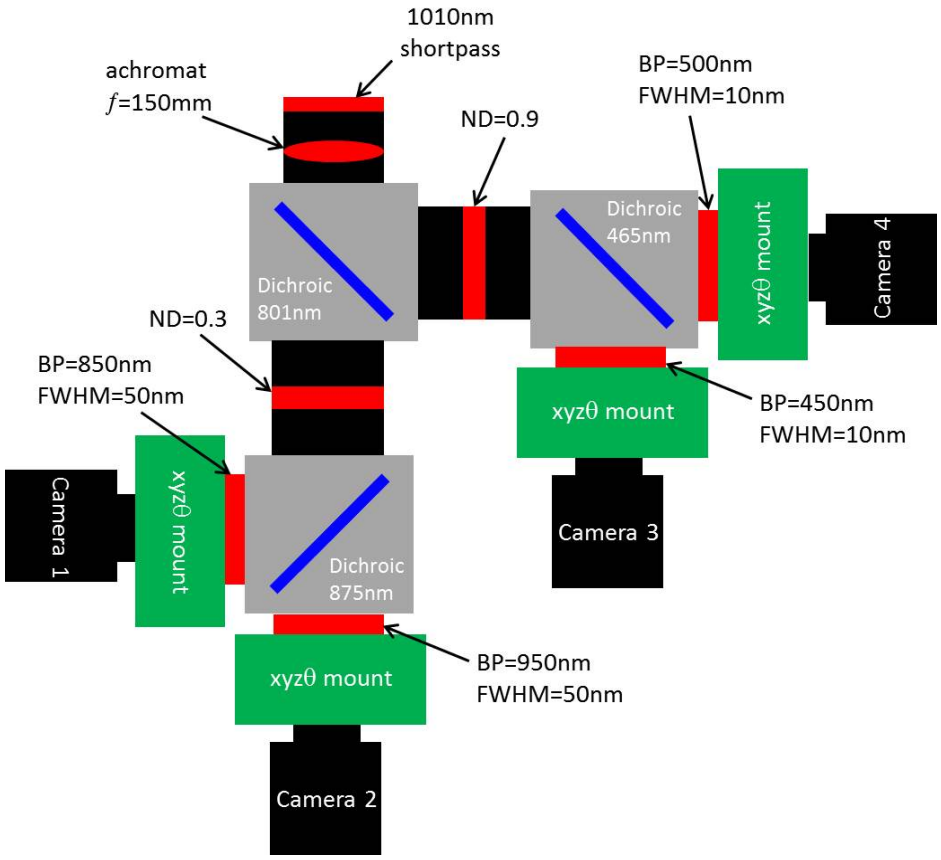

Figure 3. Schematic diagram of a 4-color pyrometer developed at Sandia. The basic design melds two, 2-color pyrometers to a common shortpass filter, achromat lens, and dichroic beamsplitter. Each 2-color channel is optimized to achieve good image registration and focus through adjustment of translation and rotation mounts. Additional registration is handled in software.

2.2.3. Optical Spectroscopy

The intense electric field at the laser focus can ionize the metal and atmospheric species and generate a plasma. By observing its optical emission, an electron (or plasma) temperature can be deduced by looking at ratios of atomic state transitions. These plasmas are considered to be optically thin (photons not readily absorbed) and in local thermodynamic equilibrium. Under these assumptions, Maxwell-Boltzmann statistics apply and collisional processes dominate over radiative ones. Thus, the population of an excited state is given by [9]

$$\frac{N_i}{N} = \frac{g_i}{Q(T)} e^{-E_i/k_B T} \quad , \tag{6}$$

where N_i is the population of the ith state with energy E_i, $Q(T)$ is the partition function, N is the total population of all states, T is the temperature, k_B is the Boltzmann constant, and g_i is the statistical weight of the ith state. The measured intensity of a transition from an upper state u to a lower state l is given by

$$I_{ul} = N_u A_{ul} h\nu_{ul}, \tag{7}$$

where N_u is the population of the upper state, A_{ul} is the transition rate, and $h\nu_{ul}$ is the energy of the transition. Substituting the Boltzmann distribution gives

$$I_{ul} = \frac{N g_u A_{ul} h\nu_{ul}}{Q(T)} e^{-E_u/k_B T} \quad . \tag{8}$$

In the Boltzmann plot method, the above equation is linearized, and the corresponding intensities of selected lines are plotted against the upper energy state E_u. The plasma temperature is then found from the slope ($-1/k_B T$) of a fit to the plotted points. The accuracy of this method relies on selecting a number of lines with large separation of the upper levels.

A simpler method that requires less computation and is more amenable to on-line monitoring estimates the plasma temperature from the intensity ratio of two lines of the same species:

$$\frac{I_1}{I_2} = \frac{g_1 A_1 \nu_1}{g_2 A_2 \nu_2} e^{-(E_1 - E_2)/k_B T} \quad . \tag{9}$$

3. EXPERIMENTS

3.1. Mundt Laser Welder

This project targeted delivery of experimental thermal data for laser welding model development. To this end, the Mundt laser welding tool at SNL (DB-2412 with IPG YLS-2000, 2kW CW ytterbium fiber laser, 1070 nm) was equipped and, in a few cases, modified with diagnostic equipment. With the 150 mm focusing lens, the measured spot size is ~280 μm at focus and ~290 μm at the normal welding position, independent of power between 300-500 W. To minimize oxidation in the open air environment, a 100 scfh argon flow gas around the nozzle was adopted.

Three cameras and a spectrometer were used to measure temperatures of the build surface and of the plasma, respectively. Figure 4 shows the various configurations used with the thermal cameras and spectrometer.

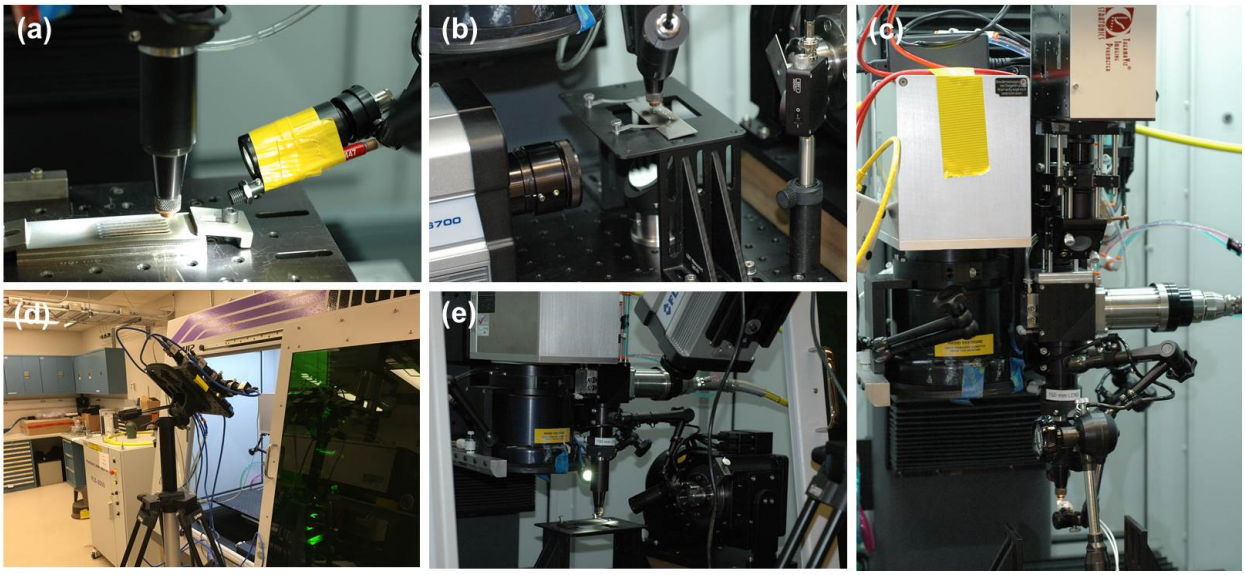

Figure 4. Experimental setups used with the Mundt laser welder. (a) Spectrometer optical input fiber (taped to housing light) at ~30° from the plate surface, (b) backside imaging with the FLIR camera using an aluminum turning mirror, (c) normal viewing with the 2-color pyrometer via a short pass filter and turning mirror, (d) tripod arrangement with the 4-color pyrometer, and (e) tripod arrangement with the FLIR camera.

The cameras consisted of a MWIR thermal camera from FLIR (SC6750, Indium Antimonide, 3-5 μm, calibrated from 250-2000 °C with ND 3 filter), a Stratonics 2-color pyrometer (silicon CMOS cameras with 750/900 nm bandpass filters, 50 nm wide, calibrated from 1000-2500 °C), and a custom 4-color pyrometer (silicon CMOS cameras with 400/500 nm and 850/950 nm bandpass filters, 10 nm and 50 nm wide respectively, calibrated from

600-2800 °C). All of these cameras were used to measure the metal surface temperatures. For measurement of the plasma temperature, a fiber spectrometer was utilized (Ocean Optics HR2000+, 1800 gr/mm, 450-575 nm bandwidth, 0.09 nm resolution, 600 μm diameter light pipe with collimating lens).

Stainless steel plates (304L) with a milled 2B finish were used for all of the temperature measurements carried out in this project (T_{melt} ~ 1450 °C). Depending on the laser power, one of two plate thicknesses was chosen, a thin plate (0.046") or a thick plate (0.13"). Figure 5 shows a few representative samples post-weld.

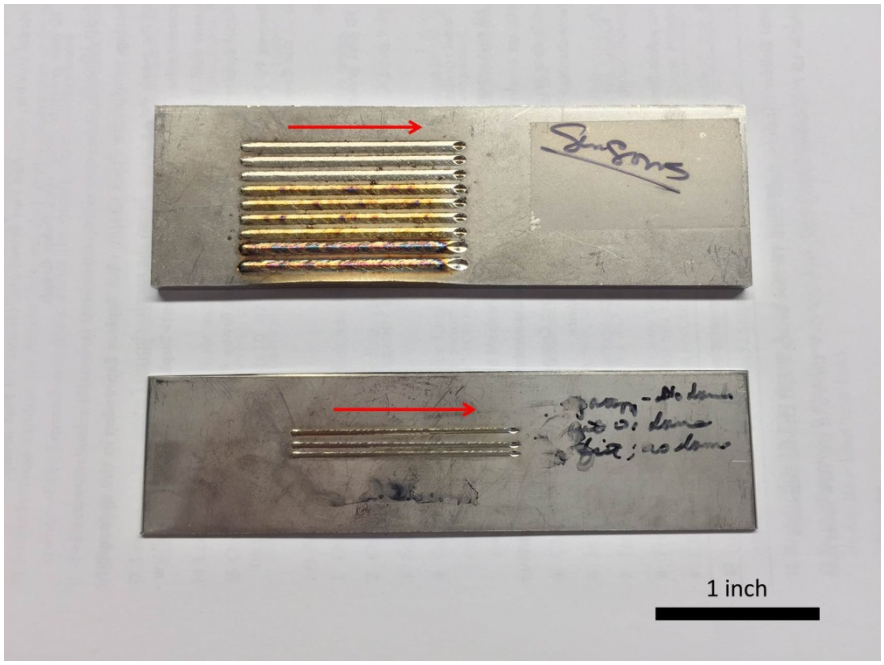

Figure 5. 304L steel plates used for laser welding thermal experiments. At top is a thick plate (0.13") on which keyhole line welds (~400 W at 40 ipm) were run; whereas, on the thin plate (0.046") below, conduction line welds (<350 W at 40 ipm) were run. Directionality is indicated by the red arrows. The rust-colored oxidation developed well after the welds were run.

3.2. Gleeble Calibration

For calibration of emissivity versus temperature, we utilized the Gleeble tool at SNL. This involved adjusting the emissivity (and thus temperature) calculated by the FLIR to match the thermocouple temperature of the heated plate. It also involved replacing the chamber window with a CaF_2 IR window, which transmits 94% of the IR radiation between 3-5 μm (Fig. 6). Thin plates with a single thermocouple placed at the center-back were mounted in the Gleeble chuck while being ramped from room temperature to ~1300 °C in

vacuum (~1×10^{-7} T) and in Ar (0.17 atm) environment. In some cases, the surfaces of the plates were coated with black paint (Rustoleum High Heat primer and paint, 248903) to fix the emissivity close to 1.

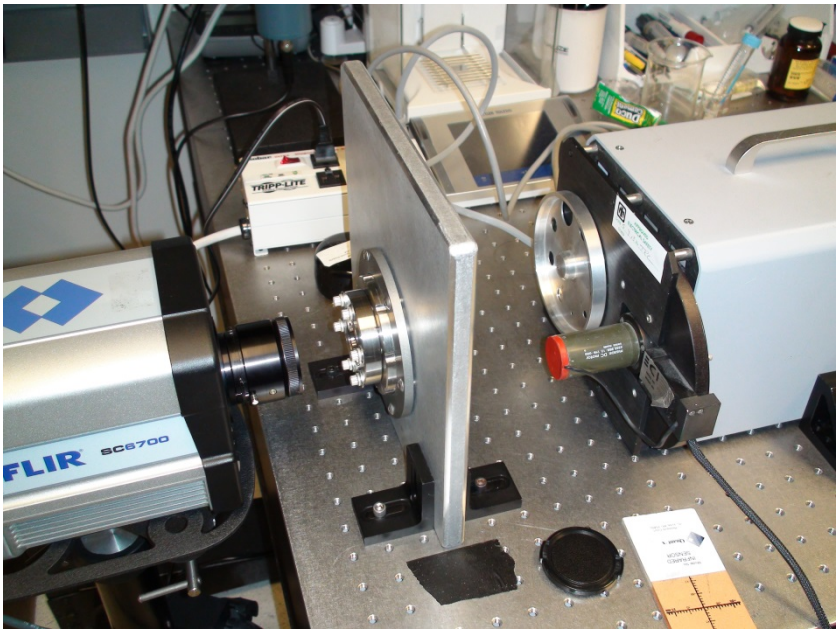

Figure 6. Calibration of the FLIR camera in the path of a CaF_2 window. The 1" window mounted in the vacuum flange bolts onto the Gleeble chamber. The path length to the blackbody source mimicked the actual distance to the heated chuck with the attached steel plate. Although done in air and only to 300°C, these differences affect the calibration of the window only minimally. From this measurement, it was determined that the window transmits 94% of the IR radiation.

4. RESULTS & DISCUSSION

This research examined laser welds on 304L stainless steel plates between 300-500 W and 8-80 ipm. The basic morphology of such a weld is shown in Fig. 7, where at 300 W the weld is conduction only but at 350 W the weld has transitioned to the deeper penetration of keyhole mode. However, the cross section seen in Fig. 7(f) does not display the characteristic teardrop shape of a keyhole weld. This is likely due to the combination of the slow speed (8 ipm) and the thin plate. Even so, the transition from conduction mode to keyhole mode occurred between 325-375 W for stage speeds over an order of magnitude, which indicates a weak dependence on stage speed.

Spectral measurements of the plasma (Fig. 8) display many discrete atomic transitions as expected of a complex alloy like 304L. On closer inspection, though, three things become apparent: 1) the background subtracted amplitude of the peaks decreases with increasing power, 2) the number of peaks does not change, and 3) the relative magnitude of the peaks does not change.

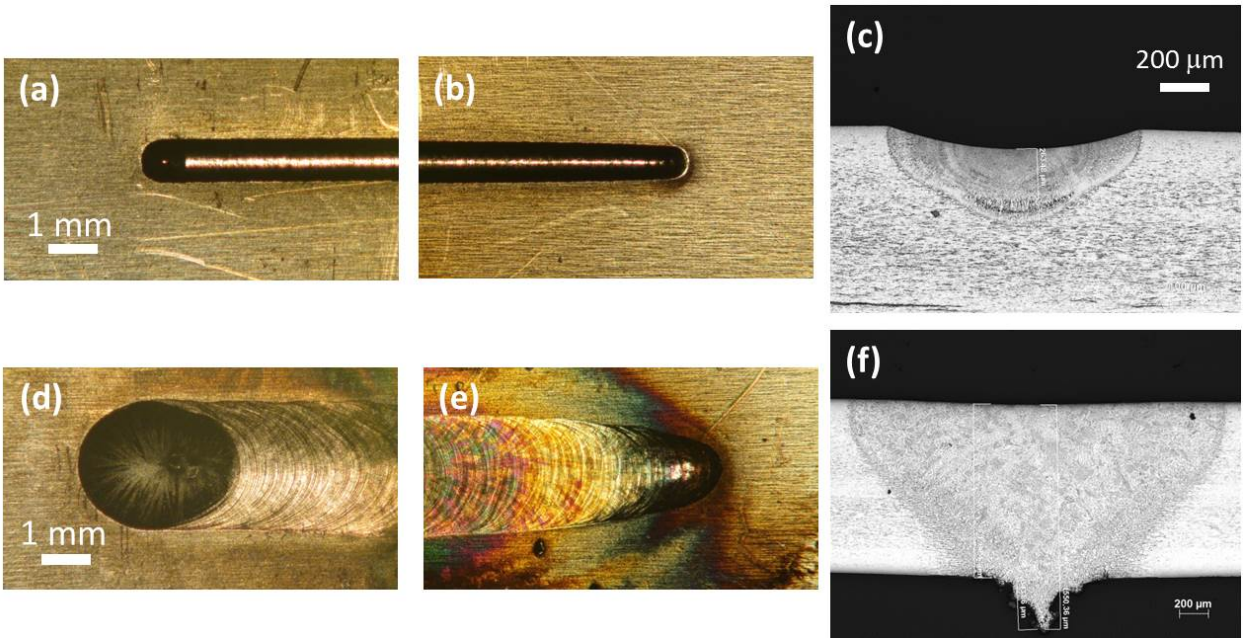

Figure 7. Morphology of laser welds on 304L plate above and below the keyhole threshold. End (a) and beginning (b) of line weld at 300 W, 8 ipm as seen by visible camera, and a cross-section (c) of the same weld as seen by a microscope. (d-f) same sequence for a 350 W, 8 ipm line weld. The plate thickness was 0.046".

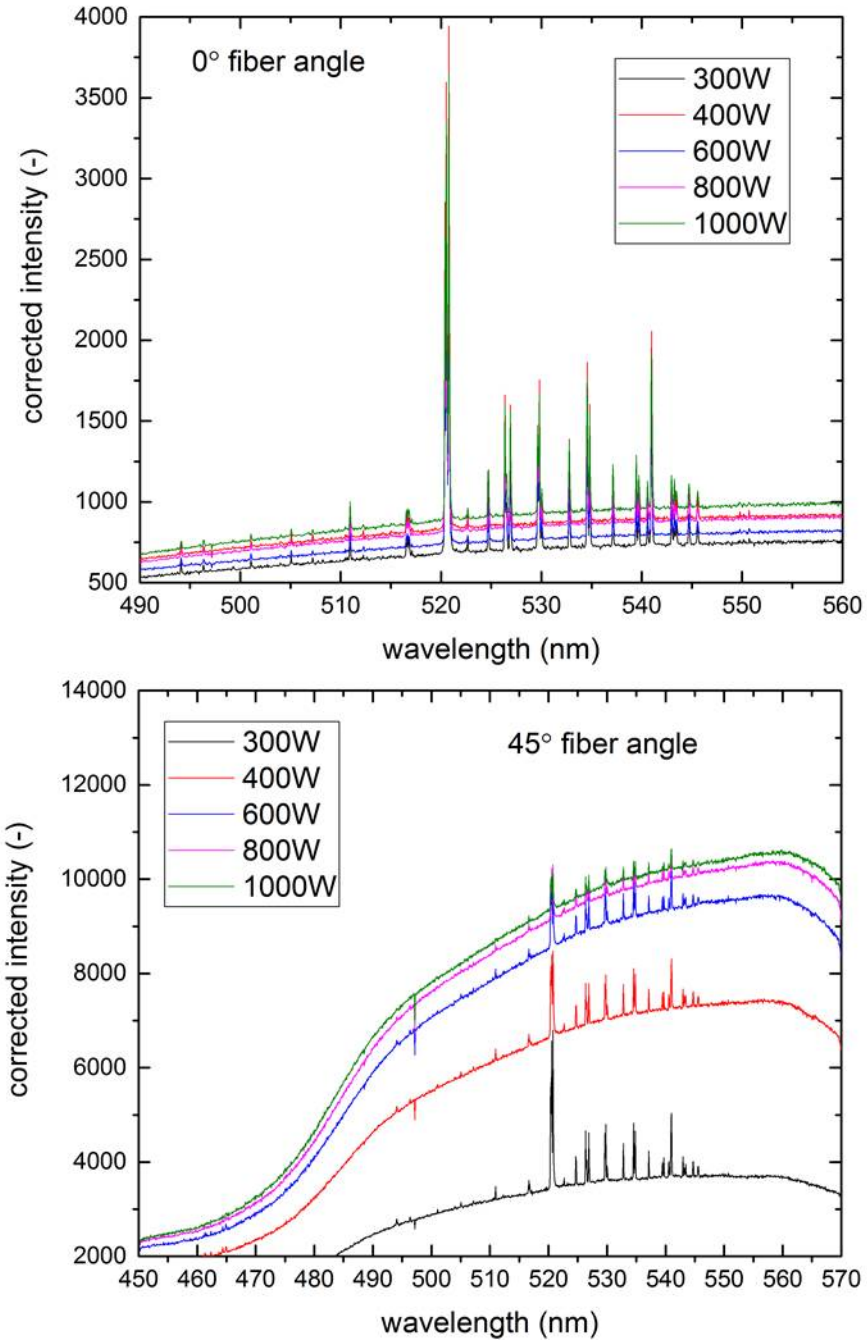

Figure 8. Measured plasma spectra for laser welds on 304L plate between 300 W and 1kW. In (a), the fiber sampled (spatially integrated) the plasma plume parallel to the surface (3" away), and in (b) the fiber captured the emission at 45° relative to the plate (3" away). The background at 45° likely originates from the continuum emission from the hot surface or molten, ejected particles.

Using the ratio method described in Section 2.2.3, plasma temperatures were calculated from a few of the identified atomic transitions of Fe and Cr. As shown in Fig. 9, the plasma temperature does not vary with laser power, but the magnitude varies by several thousands of degrees depending on which ratio is calculated. This discrepancy is due to the uncertainty of the transition parameters, the relative weakness of the lines, and to the closeness of the upper energy state. The use of the input fiber spatially integrates the plasma emission, which makes correlating plasma temperature with surface temperature impossible. However, through additional investigation it still might be possible to correlate peak surface temperature with average plasma temperature.

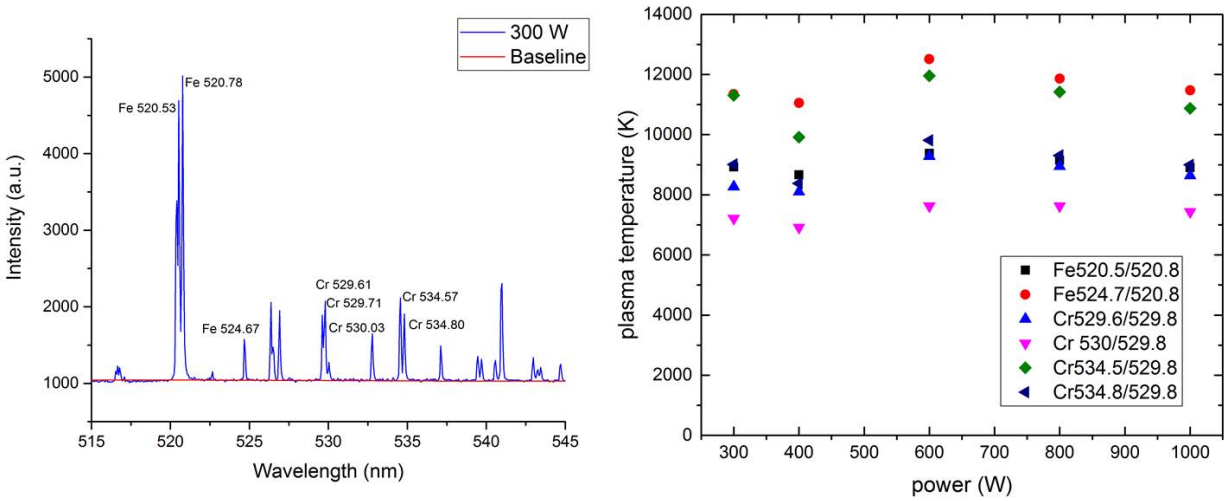

Figure 9. Spectral lines and calculated plasma temperatures for laser welds on 304L plate between 300-1000 W. Temperatures were calculated from ratios of peak intensities at the lines specified with the background subtracted.

Measuring surface temperatures underneath the plates avoided any possible interference from the plasma and also made it easier to instrument on the Mundt. This arrangement is shown in Fig. 4(b), where an aluminum turning mirror directs the emitted photons from the surface into the thermal cameras. A series of temperature profiles as measured by the FLIR and Stratonics cameras is shown in Fig. 10. As evident from the sharp rise in temperatures and shape, the transition to keyhole welding occurred around 325 W at these conditions.

Several aspects of these plots are worth noting. First, the Stratonics pyrometer acts as a melt pool (or superheated) sensor in that it captures a single exposure and from it deduces a ratio temperature. In contrast, the FLIR camera has the ability to combine (superframe) multiple images taken at different exposures and thus spans a greater

temperature range. Second, in as much as they overlap, the two cameras agree reasonably well on the shape and magnitude of the temperature. This was to be expected in this case given the presence of the high emissivity coating during the FLIR scans, which eliminates the major uncertainty in its temperature determination. And finally, the rough structure of the temperature traces at the higher powers is consistent with the cross section shown in Fig. 7(f). In this case, the power is sufficient to heat the plate completely through to a molten state and to create slag on the back side.

The temperature profiles in Fig. 10, with a sharp rise on the leading edge of the laser spot followed by a long tail behind the weld track, are consistent with profiles measured on the same side as the laser; however, it was reasoned that knowing the temperatures on the back side does not uniquely determine the front side temperatures, especially in keyhole mode. As a result, the focus shifted to measuring the melt pool and its surrounding area.

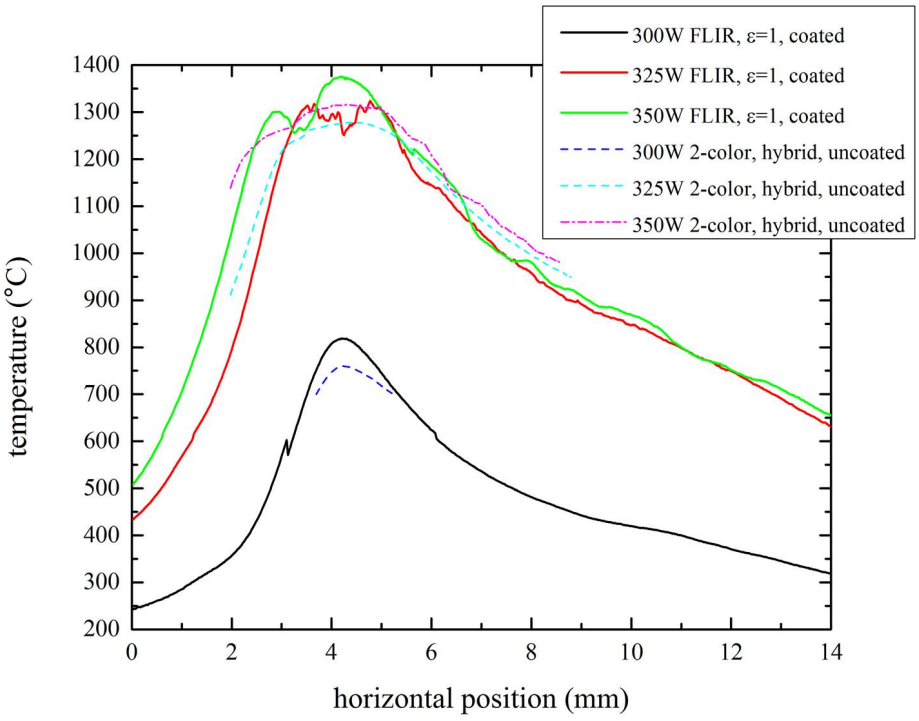

Figure 10. Backside temperatures as measured by the FLIR and Stratonics cameras along the center of the travel. Steel plates coated with high-emissivity, flat back paint were used for the IR imaging to fix the emissivity at a known value (ε~1). The powers were chosen to straddle the transition between conduction and keyhole modes. Stage speed was 8 ipm and the plate thickness was 0.046".

One aspect enjoyed by the back side, namely the known emissivity derived from the paint, disappears when moving to top side measurements because the laser burns through any coating. This motivated the use of the Gleeble instrument to calibrate the emissivity of the 304L as a function of temperature (and environmental conditions). The results of one such experiment are shown in Fig. 11. The initial drop in emissivity from 0.4 to 0.35 might be the result of outgassing of contaminants on the surface. After that, there is a steady increase, likely due to oxidation, which is inhibited by Ar. The reason for the steep drop above 1100 °C is unknown but could be due to desorption of the oxide.

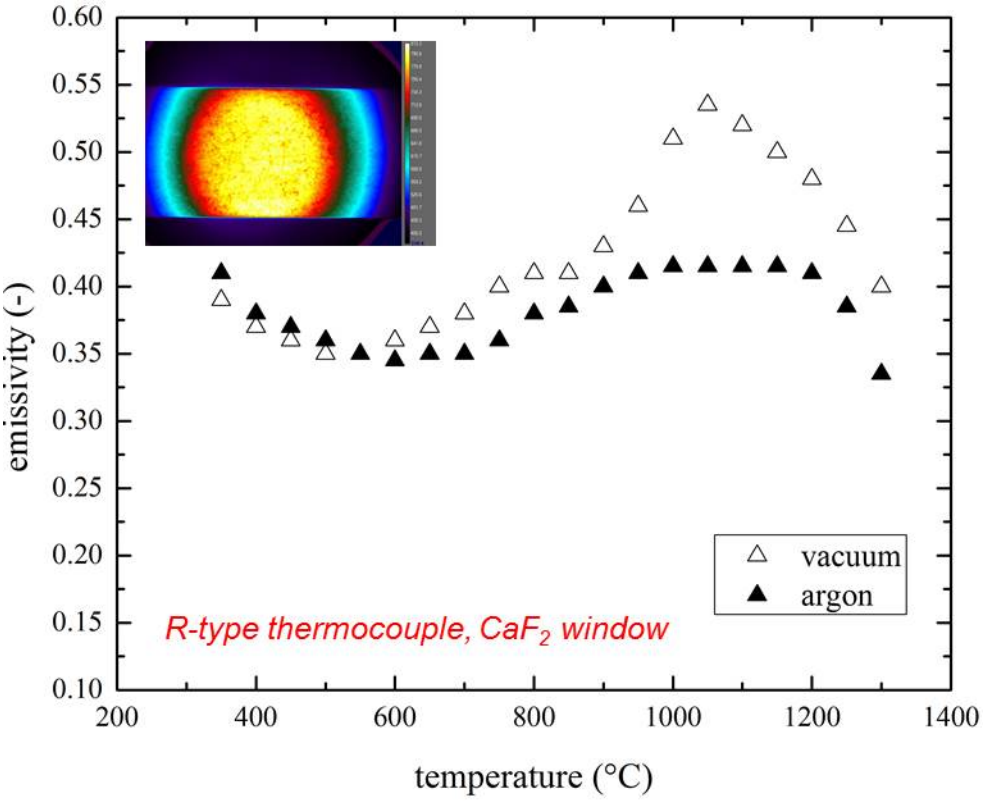

Figure 11. Gleeble measurements of 304L plate (t=0.046") with IR camera. The FLIR camera looked normally at the plate through a CaF_2 window. An R-type thermocouple was attached to the middle of the backside of the plate as a reference for the emissivity determination.

The conditions in the Mundt system do not match either the vacuum or Ar environments of the Gleeble, which makes it difficult to correlate between them. Also, the fact that the emissivity varies with temperature complicates the route to arrive at a self-consistent temperature. In such cases, the best solution is to bypass the emissivity, either through ratio pyrometry or through converting directly from raw camera counts to temperature. The latter still has the drawback of being subject to the thermal history of the part because the emissivity depends on any previous changes to the surface. In other

words, a specific count value does not uniquely determine the temperature even in identical setups if the part has been thermally cycled. Even so, during a single heating cycle, the temperature will be unique if the calibration setup exactly matches the test setup. This option has not been pursued in this project.

Both normal and side view temperatures were measured with the FLIR and Stratonics cameras as shown in the thermograms of Fig. 12. As before, the 2-color pyrometer captured only the superheated melt pool region (1500-3000 °C); whereas, the FLIR camera spanned 300-3000 °C through the use of superframing. For normal viewing with the Stratonics, the regular visible camera was removed and mounted on a fixture that transmitted light <675 nm to the visible camera and that reflected 675-1100 nm light to the pyrometer (cut further by a short pass filter that blocked the 1070 nm laser line). Simultaneous acquisition occurred with the FLIR camera mounted a tripod at a high incident angle.

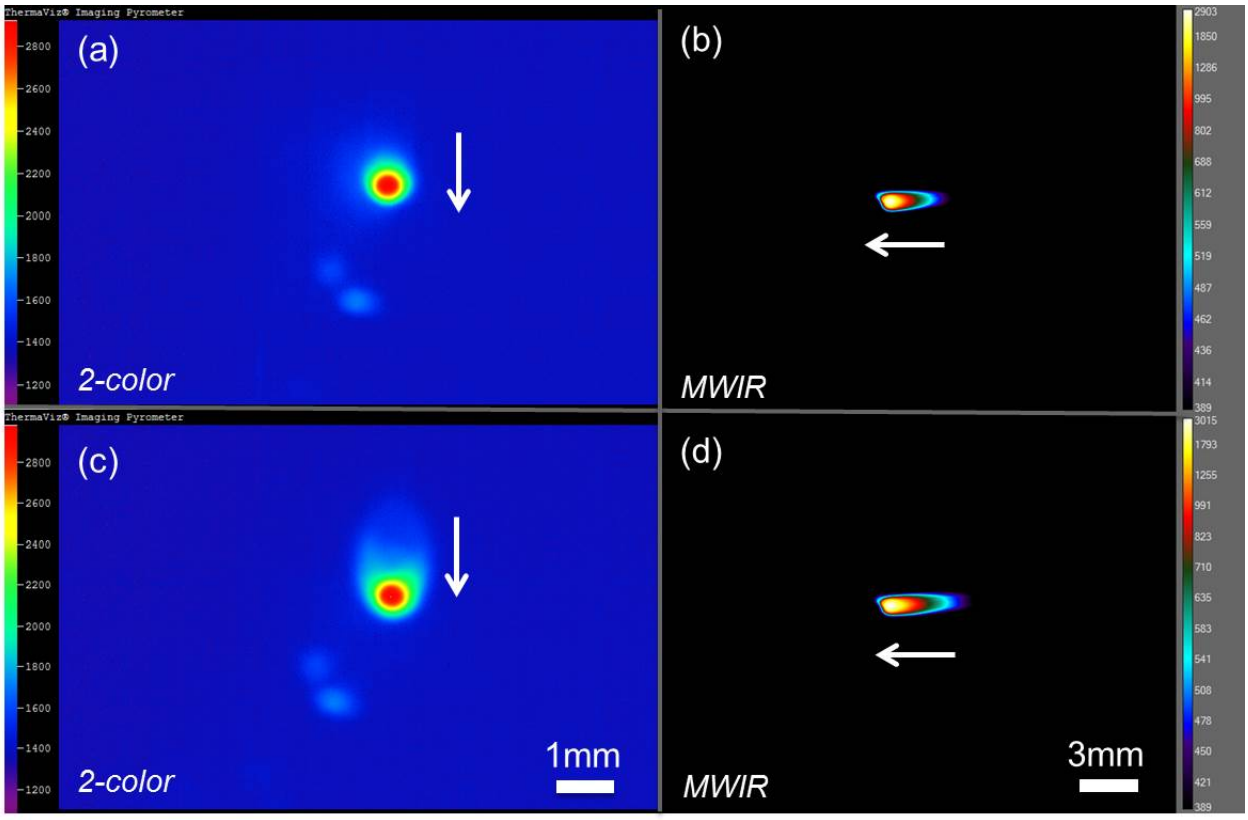

Figure 12. Thermograms of laser welds on 304L plate during conduction (*a* and *b*) and keyhole (*c* and *d*) mode welding. (a) 330 W, 80 ipm, 2-color image at normal incidence (b) 330 W, 80 ipm, IR image at 38° from normal (c) 400 W, 80 ipm, 2-color image at normal incidence, and (d) 400 W, 80 ipm, IR image at 38° from normal. Plate thickness was 0.12".

Line profiles along and perpendicular to the weld extracted from Fig. 12 are shown in Fig. 13. Here, the FLIR emissivity was set to match the peak temperature of the 2-color pyrometer (ε=0.195). This result is consistent with Ref. 10, where the emissivity above the melt temperature is lower than at any cooler temperature. As can be seen, the pyrometer consistently measures lower temperatures than the FLIR. Higher emissivities (e.g. like those found from the Gleeble experiment) would drop the calculated temperatures and bring the two cameras into better agreement. Overall, the Gleeble results follow the form predicted in Ref. 10, although with a lower point of inversion.

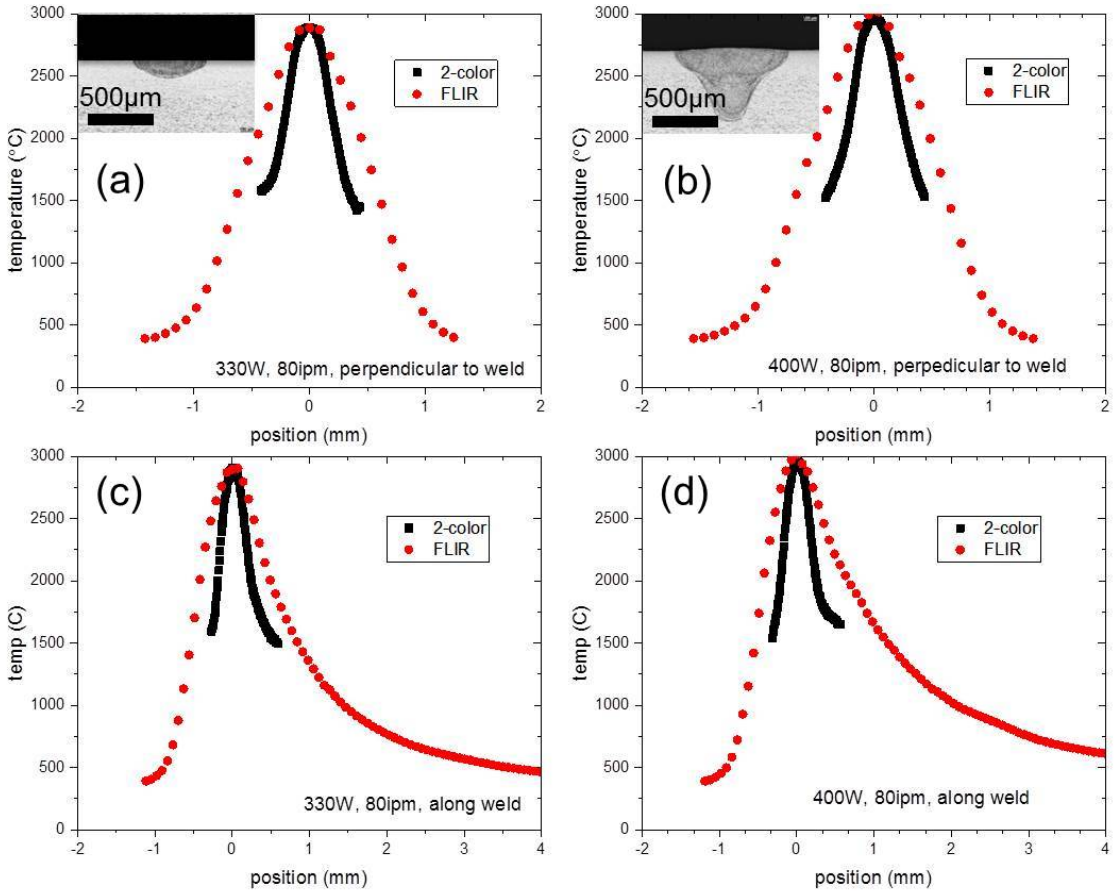

Figure 13. Measured temperature cross-sections of laser welds on 304L plate at the conditions indicated (from Fig. 12). In (a) and (b), the cut runs perpendicular to the direction of travel, while in (c) and (d), it runs along the weld at the peak temperature. Insets show the post-weld profile of the conduction (a) and keyhole (b) welds.

The 4-color pyrometer was calibrated against a NIST traceable lamp from 600-2800 °C (Fig. 14). Images of the lamp were recorded from 600-1900 °C using the 850/950 nm cameras and from 1500-2800 °C using the 450/500 nm cameras. Exposures were adjusted at each temperature to avoid saturation and matched for the 2-color pairs. To minimize non-uniformities from the lamp's helical filament, an average over a large central region was used to calculate the response at each temperature.

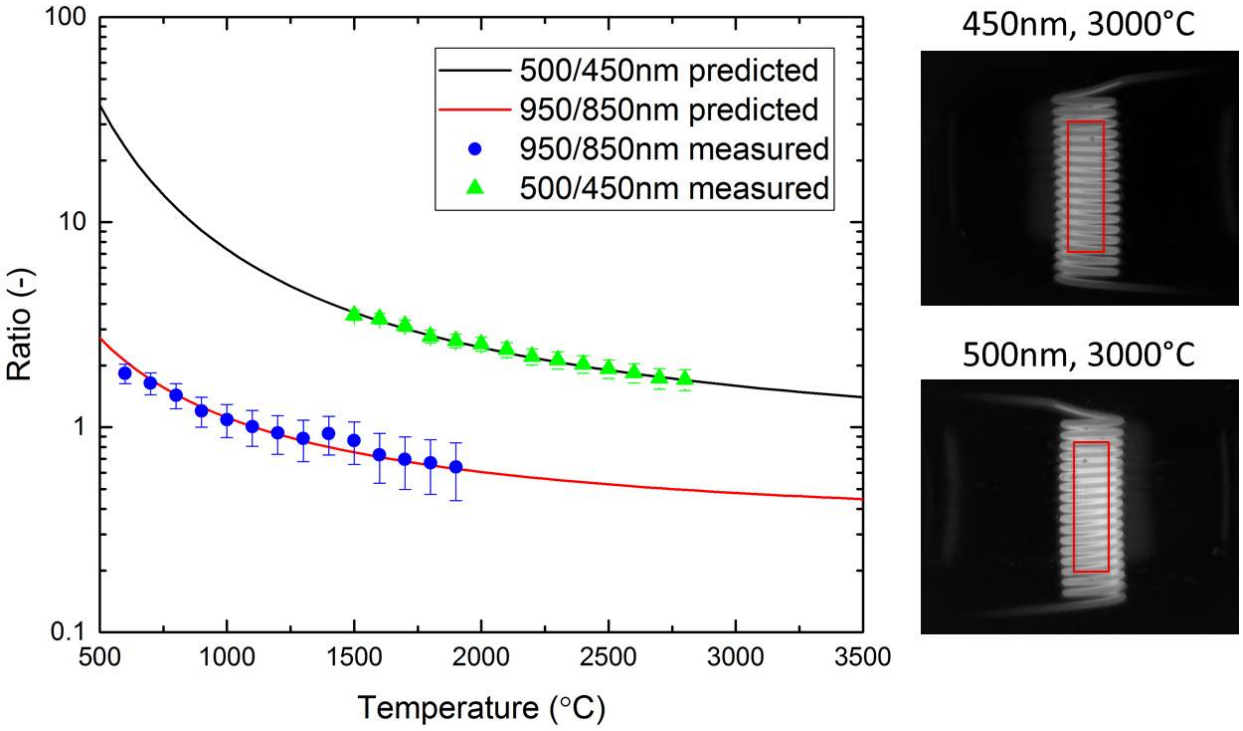

Figure 14. Calculated and measured ratio response of the 4-color pyrometer to a NIST traceable lamp. Images of the lamp at two wavelengths and 3000 °C appear on the right. An average over the red boxes was used to define the intensity. For each point, a different exposure was used, although in operation just three exposures per camera would suffice to bridge the entire 600-2800 °C temperature range.

Laser weld thermograms were calculated with the 4-color pyrometer and are shown in Fig. 15. The lower wavelength pair captured the superheated melt pool (> 2000 °C), while the long wavelength pair captured the cooler temperatures. Unlike the previous experiments welding on the flat surface of the plate, this experiment flipped the plate end on, which allowed for side views of the weld. Much more detail can be seen using the 4-color pyrometer compared to the 2-color pyrometer, including the region around the melt pool, the delineation of the solidification zone, and the plasma or hot vapor plume. However, more work with the 4-color pyrometer needs to be done; in particular, the software control does not yet automatically capture the different exposures and perform registration to build a complete composite thermogram. For

the images in Fig. 15, multiple exposures and image registration were done manually on separate weld passes; as a result, artifacts and registration errors appear. Even so, the pyrometer shows promise as a method to measure absolute temperatures similar to the Stratonics pyrometer but with a dynamic range approaching that of the FLIR camera.

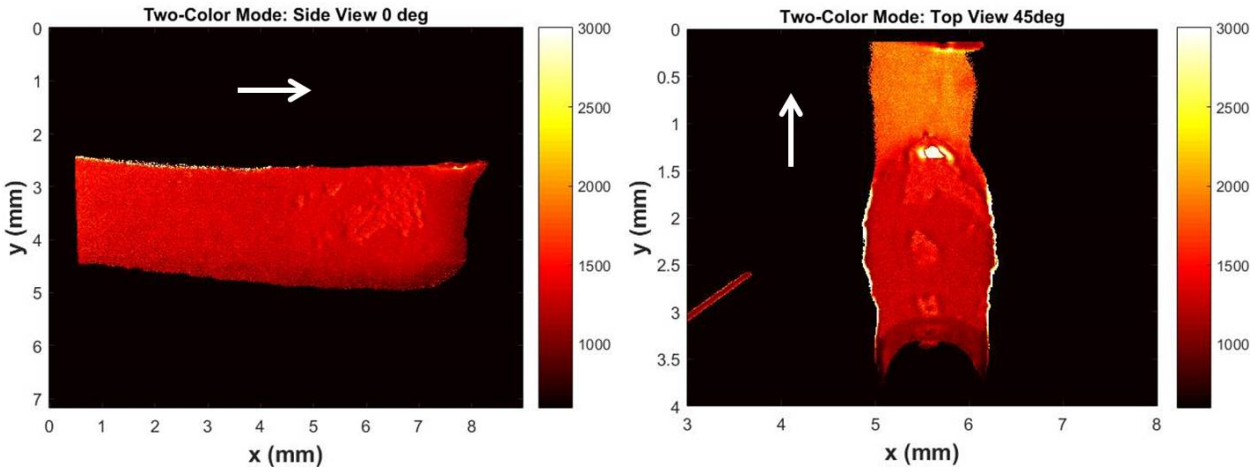

Figure 15. Thermograms of a laser weld of 304L plate (end on) taken with the 4-color pyrometer. From the side, only two temperature ranges were combined owing to the misalignment of the separate passes. From the top, three ranges were combined. Evident are the superheated region of the laser spot, the melt region around the liquidus temperature, and the solidification region. Also visible is the plasma or hot vapor plume above the surface. The side tails (white regions) are due to misalignment between passes.

5. CONCLUSION

This report summarized the multifaceted approach undertaken to measure temperatures and thermal history of laser welds on steel plates. Plasma electron temperatures were deduced from optical spectroscopy, and surface temperatures were extracted using IR thermography and multi-wavelength pyrometry. Although the plasma measurements proved challenging and not particularly enlightening, the surface measurements revealed a highly dynamic, extremely hot and variable weld region. Complementary techniques allowed for determination of temperatures over a wide range (300-3000 °C). Absolute temperatures were obtained using the 2-color pyrometer from near liquidus temperature to 3000 °C and, with the 4-color pyrometer, down to 600 °C. Relative temperatures were obtained over the entire range with the IR camera, which, when adjusted for emissivity changes with temperature, can be corrected to agree with the pyrometers. These experimental data can be used for validation, boundary condition determination, and sub-model tuning of 3D laser-weld models. Future work includes completing the software development of the 4-color camera, more accurately determining the changes in 304L emissivity with temperature, and developing new methods of measuring absolute temperatures and thermal history of dynamic processes like laser welding.

6. REFERENCES

[1] Norris, J. T., Robino, C.V., Perricone, M. J., and Hirschfeld, D. A., "Development of a Time-Resolved Energy Absorption Measurement Technique for Laser Beam Spot Welds," Welding Journal **89**, 75-81s (2010).

[2] Notz, P. K., Noble, D. R., Martinez, M. J., and Kraynik, A. M., "Use of Aria to Simulate Laser Weld Pool Dynamics for Neutron Generator Production," Technical Report, SAND2007-5870, Sandia National Laboratories (2007).

[3] Tadamalle, A. P., "Review of Real-Time Temperature Measurement for Process Monitoring of Laser Conduction Welding," Eng. Sci. Technol. An Int. J. **2**(5), 946–950 (2012).

[4] Thompson, S. M., Bian, L., Shamsaei, N.., Yadollahi, A., "An overview of Direct Laser Deposition for additive manufacturing; Part I: Transport phenomena, modeling and diagnostics," Addit. Manuf. **8**, 36–62, Elsevier B.V. (2015).

[5] Vollmer, M.., Möllmann, K.-P., [Infrared thermal imaging: fundamentals, research and applications], John Wiley & Sons (2010).

[6] Müller, B.., Renz, U., "Development of a fast fiber-optic two-color pyrometer for the temperature measurement of surfaces with varying emissivities," Rev. Sci. Instrum. **72**(8), 3366–3374 (2001).

[7] Dorsch, F., Braun, H., Keßler, S., Pfitzner, D.., Rominger, V., "Online characterization of laser beam welds by NIR-camera observation," SPIE LASE, 86030R – 86030R – 12, International Society for Optics and Photonics (2013).

[8] Dagel, D. J.,Grossetete, G. D., Maccallum, D. O., and Korey, S. P., "Four-color imaging pyrometer for mapping temperatures of laser-based metal processes," Thermosense: Thermal Infrared Applications XXXVIII, Proc. SPIE, 9861, 986103 (2016).

[9] Griem HR., [Plasma spectroscopy], McGraw-Hill (1964).

[10] Goett, G., Kozakov, R., Uhrlandt, D., Schoepp, H., and Sperl, A., "Emissivity and temperature determination on steel above the melting point," Weld World **57**, 595-602 (2013).

DISTRIBUTION

1	MS0836	Mario J. Martinez	1516
1	MS0889	Danny O. Maccallum	1831
1	MS0889	Peter S. Duran	1831
1	MS0889	Jeffrey Rodelas	1831
1	MS0889	Michael C. Maguire	1831
1	MS1085	Daryl J. Dagel	1764
1	MS1085	Grant D. Grossetete	1764
1	MS0899	Technical Library	9536 (electronic copy)


Sandia National Laboratories